

# Iterative Quantum Feature Maps

Nasa Matsumoto,<sup>\*</sup> Quoc Hoan Tran,<sup>†</sup> Koki Chinzei, Yasuhiro Endo, and Hirotaka Oshima  
*Quantum Laboratory, Fujitsu Research, Fujitsu Limited, Kawasaki, Kanagawa 211-8588, Japan*  
 (Dated: June 25, 2025)

Quantum machine learning models that leverage quantum circuits as quantum feature maps (QFMs) are recognized for their enhanced expressive power in learning tasks. Such models have demonstrated rigorous end-to-end quantum speedups for specific families of classification problems. However, deploying deep QFMs on real quantum hardware remains challenging due to circuit noise and hardware constraints. Additionally, variational quantum algorithms often suffer from computational bottlenecks, particularly in accurate gradient estimation, which significantly increases quantum resource demands during training. We propose Iterative Quantum Feature Maps (IQFMs), a hybrid quantum-classical framework that constructs a deep architecture by iteratively connecting shallow QFMs with classically computed augmentation weights. By incorporating contrastive learning and a layer-wise training mechanism, IQFMs effectively reduces quantum runtime and mitigates noise-induced degradation. In tasks involving noisy quantum data, numerical experiments show that IQFMs outperforms quantum convolutional neural networks, without requiring the optimization of variational quantum parameters. Even for a typical classical image classification benchmark, a carefully designed IQFMs achieves performance comparable to that of classical neural networks. This framework presents a promising path to address current limitations and harness the full potential of quantum-enhanced machine learning.

## I. INTRODUCTION

Transforming classical data into quantum states by leveraging the exponentially large Hilbert space accessible to quantum computers has gained attention in recent years [1, 2]. This approach draws inspiration from classical machine learning (ML), where input data is mapped into a new feature space to enhance separability. In quantum machine learning (QML), such transformations are termed quantum feature maps (QFMs). These maps arise from quantum system dynamics, driven by input data and tunable variational parameters. QFMs highlight the potential of QML, suggesting an exponential speedup due to the classical intractability of simulating certain quantum correlations [3]. For example, based on the complexity of the discrete logarithm problem, the first suggested exponential advantage in QML was demonstrated through the calculation of a support vector machine kernel matrix on a fault-tolerant quantum computer [4]. Theoretically, QFMs could enable QML models to serve as universal approximators of continuous functions [5]. It is also possible to design specialized data sets that show the significant differences between quantum and classical models from a learning theory perspective, thereby illustrating the quantum advantage in ML problems [6]. However, finding similar advantages in practical applications, particularly those feasible for near-term quantum computers, remains challenging.

The selection of QFMs is often aimed at boosting the quantum model’s performance, where typically these maps are neither optimized nor trained. One could use deep quantum circuits to construct a QFM, but this ap-

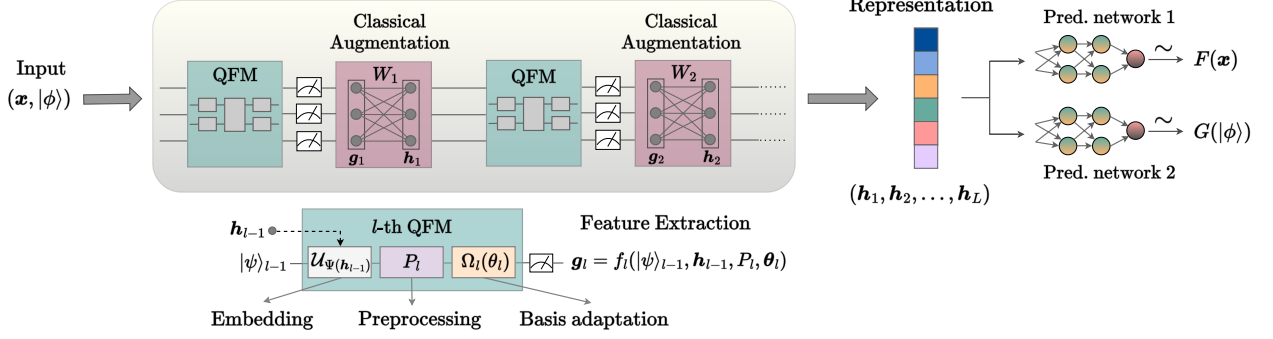
proach does not align well with the capabilities of near-term quantum computers, which are susceptible to noise and prone to errors. A common strategy is to append variational quantum circuits (VQCs) after the feature map circuit, forming the structure of a quantum neural network (QNN). This design aims to create more expressive circuits for quantum algorithms. However, training such circuits [7] through variational quantum algorithms (VQAs) often runs into issues like becoming stuck in local minima [8, 9] or encountering plateau regions [10–12], making it hard to find optimal solutions. Despite some QNN designs showing resilience to the barren plateaus phenomenon, evidence indicates that the loss functions of these models may be classically simulated if classical data from quantum devices are gathered during an initial phase [11, 13–15]. This underscores the importance of developing QML models that are not only highly trainable but also practically useful or capable of achieving quantum advantages beyond classical simulation capabilities. Moreover, combined with the lack of efficient gradient estimation algorithms [16, 17], it is argued that VQAs may struggle to surpass classical approaches in terms of time scaling to demonstrate quantum advantages with the current QML models [18]. This analysis points towards a more natural form of hybrid quantum-classical algorithms that can integrate the strengths of both quantum and classical ML models.

In this paper, we introduce Iterative Quantum Feature Maps (IQFMs), a hybrid quantum-classical framework designed to minimize the quantum resources needed for learning compared to a deep QFM. IQFMs features a deep architecture that iteratively connects shallow quantum circuits as QFMs. This design enhances expressiveness by linking each QFM to the next via measurement outputs, which are then processed through classical augmentation [Fig. 1(a)]. QFM outputs are mea-

<sup>\*</sup> [matsumoto.nasa@fujitsu.com](mailto:matsumoto.nasa@fujitsu.com)

<sup>†</sup> [tran.quochoan@fujitsu.com](mailto:tran.quochoan@fujitsu.com)

### (a) Iterative Quantum Feature Maps (IQFMs)



### (b) Representation Learning

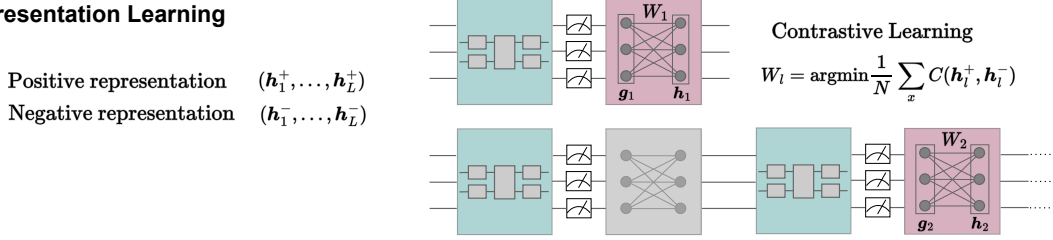


FIG. 1: IQFMs and the representation learning in processing classical input  $\mathbf{x}$  and quantum input  $|\phi\rangle$ . (a) The  $l$ -th QFM starts with a quantum state  $|\psi\rangle_{l-1}$  and uses an embedding circuit  $\mathcal{U}_{\Psi(\mathbf{h}_{l-1})}$  to map classical features  $\mathbf{h}_{l-1}$  into a quantum state, followed by a preprocessing circuit  $P_l$ , then a parameterized circuit  $\Omega_l(\boldsymbol{\theta}_l)$  to adapt the measurement basis. Extracted features  $\mathbf{g}_l$  from the  $l$ -th QFM are passed to the  $(l+1)$ -th QFM through classical augmentation with trainable weights. The outputs  $\mathbf{h}_l$  from all augmentation layers are aggregated into a classical feature vector, which is fed into multiple prediction networks to predict properties of  $\mathbf{x}$  and  $|\phi\rangle$ . (b) IQFMs employs contrastive learning to train the classical augmentation weights sequentially, leaving quantum circuit parameters fixed. Here, positive representations  $(\mathbf{h}_1^+, \dots, \mathbf{h}_L^+)$  are derived from data similar to the input (e.g., perturbed versions or same-class samples), while negative representations  $(\mathbf{h}_1^-, \dots, \mathbf{h}_L^-)$  come from dissimilar data (e.g., different-class samples). For each layer  $l$ , the weight  $\mathbf{W}_l$  is trained to minimize the cost function  $\mathcal{C}(\mathbf{h}_l^+, \mathbf{h}_l^-)$ , which pulls positive representations closer and pushes negative representations away. This process begins with  $\mathbf{W}_1$ , fixes it, then trains  $\mathbf{W}_2$ , and continues layer by layer until the final layer, then repeating until termination conditions are met.

sured across multiple bases, ensuring stability in deeper layers through normalized classical augmentation. The outputs from all augmentation layers are aggregated into a classical feature vector, which is suitable for multiple tasks such as classification or regression using other classical neural networks (NNs) for prediction. Unlike conventional methods that train the parameters of quantum circuits, IQFMs optimizes only the weights of the classical augmentation that links the QFMs to produce effective feature vectors. By employing contrastive learning [19–23] and a layer-by-layer training approach to adjust these classical weights, IQFMs reduces quantum computational runtime and mitigates the impact of noise [Fig. 1(b)]. The framework is versatile, supporting both quantum and classical data classification tasks. Numerical experiments in our study demonstrate that IQFMs is effective for both classical data and quantum data. In classifying quantum phases of matter using noisy quantum data, IQFMs outperforms the quantum convolutional neural network (QCNN) model [24–26] without re-

quiring the optimization of variational quantum parameters. In classifying image data, IQFMs achieves accuracy comparable to that of similar classical architectures.

## II. METHODS

### A. Iterative Quantum Feature Maps (IQFMs)

IQFMs employs a deep structure that enhances the connectivity of QFMs by applying classical augmentation to the measurement outcomes before moving to the subsequent QFM. The  $l$ -th QFM block starts from the input quantum state  $|\psi\rangle_{l-1}$ , applies a feature map circuit  $\mathcal{U}_{\Psi(\mathbf{h}_{l-1})}$  to embed the classical data  $\mathbf{h}_{l-1}$  into the quantum state  $|\Psi(\mathbf{h}_{l-1})\rangle$ , then uses a fixed preprocessing circuit  $P_l$  to entangle and mix the data, and applies measurement basis adaptation circuit  $\Omega_l(\boldsymbol{\theta}_l)$  parameterized by  $\boldsymbol{\theta}_l$  to rotate the state into an optimal measurement basis. This process yields

$|\Psi(\mathbf{h}_{l-1}, P_l, \boldsymbol{\theta}_l)\rangle = \Omega_l(\boldsymbol{\theta}_l) P_l \mathcal{U}_{\Psi(\mathbf{h}_{l-1})} |\psi\rangle_{l-1}$  [Fig. 1(a)]. The sequential repetition of the combination of  $\mathcal{U}_{\Psi(\mathbf{h}_{l-1})}$ ,  $P_l$ , and  $\Omega_l(\boldsymbol{\theta}_l)$ , with varying parameters  $\boldsymbol{\theta}_l$ , is known as the data re-uploading framework [27]. The feature extraction via measurements yields a feature vector  $\mathbf{g}_l = f_l(|\psi\rangle_{l-1}, \mathbf{h}_{l-1}, P_l, \boldsymbol{\theta}_l) \in \mathbb{R}^{d_g}$ , where  $d_g$  is the number of extracted features. In general,  $f_l(|\psi\rangle_{l-1}, \mathbf{h}_{l-1}, P_l, \boldsymbol{\theta}_l)$  can be constructed from measurement records. Here, we restrict its implementation to the expectation values of measurement operators, i.e.,  $[f_l(|\psi\rangle_{l-1}, \mathbf{h}_{l-1}, P_l, \boldsymbol{\theta}_l)]_j = \langle \Psi(\mathbf{h}_{l-1}, P_l, \boldsymbol{\theta}_l) | O_j | \Psi(\mathbf{h}_{l-1}, P_l, \boldsymbol{\theta}_l) \rangle$ , where  $O_j$  is the observable associated with the  $j$ th feature.

IQFMs with  $L$  layers is constructed as follows:

1. At the layer  $l = 1$ , the QFM is initialized with a quantum data  $|\psi\rangle_0$  and a classical data  $\mathbf{h}_0$ .
2. For each layer  $l = 1, \dots, L$ , the following operations are performed:

$$\mathbf{g}_l = f_l(|\psi\rangle_{l-1}, \mathbf{h}_{l-1}, P_l, \boldsymbol{\theta}_l) \in \mathbb{R}^{d_g}, \quad (1)$$

$$\mathbf{h}_l = \mathcal{A}_l(\mathbf{W}_l, \mathbf{g}_l) \in \mathbb{R}^{d_h}. \quad (2)$$

Here, Eqs. (1) and (2) represent the quantum feature extraction via the QFM of the  $l$ th layer and the classical augmentation  $\mathcal{A}_l$  with parameters  $\mathbf{W}_l$  (such as a classical neural network), respectively. Additionally,  $|\psi\rangle_{l-1}$  represents the input quantum state for the  $l$ -th QFM. If  $|\psi\rangle_{l-1} = |\psi\rangle_0$  for  $l = 1, 2, \dots$ , IQFMs adopts a re-input structure. For ease of analysis, we consider the dimensions of  $\mathbf{g}_l$  and  $\mathbf{h}_l$  as  $d_g$  and  $d_h$ , respectively, to be constant across layers. At each layer  $l$ , there are two sets of parameters involved:  $\boldsymbol{\theta}_l$  for the quantum circuit and  $\mathbf{W}_l$  for the classical augmentation, corresponding to the quantum feature extraction and classical processing steps, respectively. This work assumes that  $\mathbf{W}_l$  is trainable while  $\boldsymbol{\theta}_l$  is fixed to random values.

The above structure enables IQFMs to process both classical and quantum data, enhancing its versatility and near-term applicability on quantum devices. In an ML task involving both classical input  $\mathbf{x}$  and quantum input  $|\phi\rangle$ , our QML model needs to approximate a true hybrid function  $\mathcal{F}(\mathbf{x}, |\phi\rangle)$ . This encompasses scenarios with solely classical input or solely quantum input. For instance, when IQFMs processes only classical data  $\mathbf{x}$ , we set  $\mathbf{h}_0 = \mathbf{x}$  and fix the quantum state  $|\psi\rangle_0$  (e.g.,  $|0\rangle^n$ ) to approximate a target function  $F(\mathbf{x})$ . Conversely, when IQFMs processes only the quantum state  $|\phi\rangle$ , we set  $|\psi\rangle_0 = |\phi\rangle$  and fix the classical data  $\mathbf{h}_0 \in \mathbb{R}^{d_h}$  to approximate a target function  $G(|\phi\rangle)$  (Fig. 1).

When inputting a quantum state into IQFMs, a preprocessing circuit  $P_l$  plays a crucial role. Feeding  $|\psi\rangle_{l-1}$  into the  $l$ -th QFM without preprocessing may lead to loss of specific features of the quantum state information. The preprocessing circuit enhances the distinguishability of these relevant features before measurement. Furthermore, the re-input structure,  $|\psi\rangle_{l-1} = |\phi\rangle$  for  $l = 1, 2, \dots$ , can be essential for IQFMs, especially in deep architectures. If the input quantum data  $|\phi\rangle$  is set only as the input state of the first layer  $|\psi\rangle_0 = |\phi\rangle$ , then as the depth of

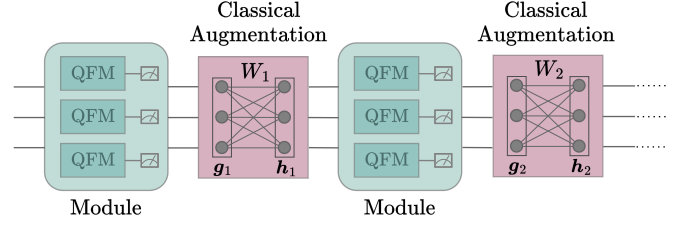


FIG. 2: The modular IQFMs. The classical data  $\mathbf{h}$  is partitioned and processed in parallel by multiple QFMs within each module. The resulting feature vectors of QMFs in each module are then combined and forwarded to the next layer.

the IQFMs layers increases, there may be insufficient information transmission. The re-input structure addresses this issue by setting  $|\psi\rangle_{l-1} = |\phi\rangle$  for  $l = 1, 2, \dots$ , ensuring consistency of the quantum state input across all layers. This promotes learning stability in the deeper layers.

Remarkably, IQFMs can be defined on a modular architecture, in which the classical data  $\mathbf{h}$  is partitioned into multiple parts and processed in parallel by multiple QFMs within a single module (Fig. 2). The resulting feature vectors for each module are then combined, augmented, and forwarded to the QFMs in the next layer. This modular architecture enables more flexible and expressive models that are capable of capturing complex patterns and relationships in data. The processing pipeline falls under the general definition in Eqs. (1) and (2), assuming the embedding, preprocessing, and measurement basis adaptation circuits are disentangled into multiple subcircuits. Due to this modular design, the entire quantum circuit does not need to be executed on a quantum device at once. Instead, only the individual subcircuits need to be implemented, making it feasible to address large-scale learning tasks even on near-term quantum devices with limited qubit resources.

## B. Quantum Feature Extraction

Quantum feature extraction in the QFM involves performing quantum measurements in multiple bases to extract richer features. We consider a scenario where an experimenter has access to multiple copies of the  $n_q$ -qubit preprocessed state  $|\pi\rangle = P\mathcal{U}_{\Psi(\mathbf{h})} |\psi\rangle$  of the QFM. The experimenter can perform a limited set of quantum measurements across multiple bases, denoted by a collection of Positive Operator-Valued Measurements (POVMs),  $\{\mathcal{M}_k\}$ , where each  $\mathcal{M}_k = \{M_{k,j}\}$  corresponds to a specific measurement basis labeled by  $k$ . Here, a POVM is a mathematical tool used in quantum mechanics to describe the possible outcomes of a measurement. The operators  $M_{k,j}$  act on the system's Hilbert space and satisfy the normalization condition  $\sum_j M_{k,j} = I$  for each  $k$ , en-

sure that the probabilities of all possible outcomes sum to 1. For a given POVM  $\mathcal{M}_k$ , the experimenter measures a subset of the copies of  $|\pi\rangle$  in the corresponding basis. The probability of obtaining outcome  $j$  in basis  $k$  is given by the Born rule:  $p(j) = \text{Tr}(|\pi\rangle\langle\pi| M_{k,j})$ . Given an observable  $O^{(k)}$  associated with the measurement outcomes in the basis  $k$ , the expectation value is computed as:

$$\langle O^{(k)} \rangle = \sum_j o_{k,j} p_k(j), \quad (3)$$

where  $o_{k,j}$  is the numerical value of the observable  $O^{(k)}$  corresponding to outcome  $j$  in basis  $k$ . The experimenter repeats this measurement process over many copies of  $\rho$  to estimate the probabilities  $p_k(j)$  and compute  $\langle O^{(k)} \rangle$ .

Given a set of observables  $\{O_1^{(k)}, \dots, O_F^{(k)}\}$  associated with the measurement bases, the experimenter collects statistics from each basis  $k$ , such as the expectation values  $g_i^{(k)} = \langle O_i^{(k)} \rangle$ , over the index  $i \in \{1, \dots, F\}$ . These values form a feature vector  $\mathbf{g}^{(k)} = (g_1^{(k)}, \dots, g_F^{(k)}) \in \mathbb{R}^F$ . Employing multiple measurement bases can distinguish quantum and classical generative models [28, 29] and may enhance QFM's classification performance. This approach also prevents classical simulation of Pauli-Z words expectation values for specific circuit classes [30].

We define basis  $k = 0$  as the computational basis, where each  $O_i^{(0)} = Z^{i_1} \otimes \dots \otimes Z^{i_{n_q}}$  ( $\{i_1, \dots, i_{n_q}\} \in \{0, 1\}^{n_q}$ ) is a Pauli-Z word chosen from  $2^{n_q}$  possible Pauli-Z words. Here, the measurement is performed on  $|\pi\rangle$  without the basis adapting circuit  $\Omega(\theta)$ . To enrich the feature set, we perform measurements in additional bases, each indexed by  $k$ , yielding a feature vector  $\mathbf{g}^{(k)}$ . This is accomplished by applying a well-selected  $\Omega(\theta^k)$  to  $|\pi\rangle$  before measuring it in a computational basis, corresponding to  $O_i^{(k)} = \Omega^\dagger(\theta^k) O_i^{(0)} \Omega(\theta^k)$ . The circuit  $\Omega(\theta^k)$  can be a random Clifford or a random local circuit, such as layers of random single-qubit rotations and two-qubit gates on neighboring qubits. To prioritize practicality, we implement  $\Omega(\theta^k)$  as a product of single-qubit rotations,  $\Omega(\theta^k) = \prod_{j=1}^{n_q} RX(\theta_j^k)$ , where  $\theta_j^k$  is a randomly fixed angle. The feature for each QFM is a concatenation of  $\mathbf{g}^{(0)}$  with  $\mathbf{g}^{(1)}, \dots, \mathbf{g}^{(B)}$ , derived from other  $B$  distinct bases (Fig. 3):  $\mathbf{g} = (\mathbf{g}^{(0)}, \mathbf{g}^{(1)}, \dots, \mathbf{g}^{(B)}) \in \mathbb{R}^{d_g}$ , where  $d_g = (B+1)F$ .

In IQFMs, the final representation vector is formed by augmenting  $\mathbf{g}_l$  as  $\mathbf{h}_l = \mathcal{A}(\mathbf{W}_l, \mathbf{g}_l) \in \mathbb{R}^{d_h}$  with the classical weights  $\mathbf{W}_l$  and concatenating them from all layers into  $\mathbf{h} = (\mathbf{h}_1, \dots, \mathbf{h}_L) \in \mathbb{R}^{d_{hL}}$ . This representation vector  $\mathbf{h}$  can be utilized for downstream tasks such as classification and regression. For example, a trainable classical neural network  $\mathcal{N}$  can process  $\mathbf{h}$  to approximate the target functions, e.g.,  $\mathcal{N}(\mathbf{h}) \sim F(\mathbf{x})$  or  $\mathcal{N}(\mathbf{h}) \sim G(|\phi\rangle)$  [Fig. 1(a)]. Numerical experiments in our study reveal that, in most cases, only training  $\mathcal{N}$  without learning  $\mathbf{W}_l$  cannot reach sufficient accuracy in classification tasks. This demonstrates that further representation learning is required to enhance the separability of  $\mathbf{h}$  across distinct input labels.

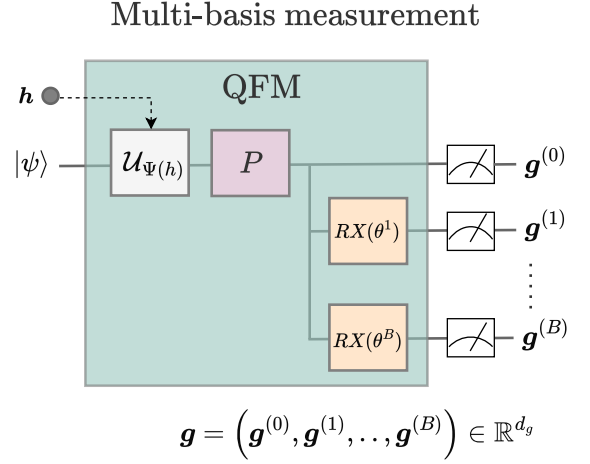


FIG. 3: The quantum feature extraction involves multi-basis measurement. The initial feature vector  $\mathbf{g}^{(0)}$  is derived from all qubits measurement in the Z-basis. To expand the feature set, measurements are performed on other  $B$  distinct bases to acquire  $\mathbf{g}^{(1)}, \dots, \mathbf{g}^{(B)}$ . Here,  $\mathbf{g}^{(i)}$  is obtained by applying a random single-qubit rotation  $RX(\theta^i)$  to all qubits. The total extracted feature vector  $\mathbf{g}$  is a concatenation of  $\mathbf{g}^{(0)}, \dots, \mathbf{g}^{(B)}$ .

### C. Representation Learning

Quantum circuit learning [7] focuses on optimizing the parameters of quantum circuits, whereas IQFMs training targets the parameters of classical augmentation  $\mathbf{W}_l$  without adjusting the quantum circuit parameters. However, training these classical parameters using a conventional approach, such as defining a loss function based on the final output of IQFMs and the target of ML tasks and then updating the parameters via its gradient, still necessitates computing the gradient of the QFM output. This is a computationally expensive process that we aim to avoid. To estimate the quantum resources required for this training, we fix the size of the training set, the number of measurement shots per feature extraction, and the per-layer circuit runtime. Let  $T$  denote the number of training epochs and consider the loss function  $\mathcal{L} = \mathcal{L}(\mathbf{h}_1, \dots, \mathbf{h}_L)$ , where each augmented feature  $\mathbf{h}_l \in \mathbb{R}^{d_h}$  is produced in the  $l$ th layer. The gradient with respect to  $\mathbf{W}_l$  can be written as

$$\begin{aligned} \frac{\partial \mathcal{L}}{\partial \mathbf{W}_l} &= \sum_{k=l}^L \frac{\partial \mathcal{L}}{\partial \mathbf{h}_k} \frac{\partial \mathbf{h}_k}{\partial \mathbf{W}_l} \\ &= \sum_{k=l}^L \frac{\partial \mathcal{L}}{\partial \mathbf{h}_k} \left( \prod_{m=l+1}^k \frac{\partial \mathbf{h}_m}{\partial \mathbf{h}_{m-1}} \right) \frac{\partial \mathbf{h}_l}{\partial \mathbf{W}_l} \\ &= \sum_{k=l}^L \frac{\partial \mathcal{L}}{\partial \mathbf{h}_k} \left( \prod_{m=l+1}^k \frac{\partial \mathbf{h}_m}{\partial \mathbf{g}_m} \frac{\partial \mathbf{g}_m}{\partial \mathbf{h}_{m-1}} \right) \frac{\partial \mathbf{h}_l}{\partial \mathbf{W}_l}, \quad (4) \end{aligned}$$



where  $\mathbf{g}_m \in \mathbb{R}^{d_g}$  is the quantum-extracted feature vector at layer  $m$ . The terms  $\partial\mathcal{L}/\partial\mathbf{h}_k$ ,  $\partial\mathbf{h}_m/\partial\mathbf{g}_m$ , and  $\partial\mathbf{h}_l/\partial\mathbf{W}_l$  can be computed classically, so the only quantum-costly Jacobian is  $\partial\mathbf{g}_m/\partial\mathbf{h}_{m-1}$ . Using the parameter-shift rule [7, 31], evaluating this  $d_g \times d_h$  Jacobian requires  $O(d_h d_g)$  circuit executions per layer. Summing over  $L$  layers and  $T$  training epochs yields a total quantum-resource scaling of  $O(T L d_h d_g)$ .

Alternatively, IQFMs can be employed without training any parameters, transforming it into a quantum extreme learning machine (QELM) [32, 33], although this may introduce some drawbacks. In the QELM, internal parameters are typically randomized, and the extracted features are fed into a trainable readout layer for classification or regression tasks. The rationale for using QELM lies in leveraging quantum dynamics as a quantum reservoir [34–37] to generate a high-dimensional feature space suitable for ML tasks, bypassing the challenges of training internal dynamics. The classical augmentation can be viewed as a higher-order connection [38] that enhances the computational power of quantum reservoirs. As internal parameters require no training, quantum resources are utilized solely for feature extraction, resulting in a computational cost of  $O(L d_g)$ . However, this approach is sensitive to the dynamical regime, lacks robustness against noise, and may fail to ensure input separability, as evidenced by our numerical experiments.

To address the challenge of using IQFMs as QELM, we propose a representation learning algorithm for IQFMs to obtain extracted features with high input separability. In the applications, we perform two steps: Step 1 involves representation learning up to  $T$  epochs to refine the extracted features, while Step 2 trains the readout layer for classification or regression tasks using these features.

The representation learning leverages contrastive learning and a layer-by-layer training strategy to optimize its classical augmentation components [Fig. 1(b)]. The key idea of IQFMs lies in training the classical augmentation components during representation learning without computing the gradient of the QFM output. This scheme does not remove the optimization of internal parameters as QELM but eliminates the dependency of quantum resources on the number of parameters during optimization, reducing the quantum computational runtime to  $O(T L d_g)$ .

Contrastive learning [19–23], a well-established ML technique, constructs an embedding space where similar sample pairs are positioned closely together, while dissimilar pairs are separated by greater distances. This method enhances the ability to discern meaningful patterns in the data by emphasizing relative relationships between samples rather than absolute values. In the context of IQFMs, contrastive learning strengthens robustness to noise, which is crucial in quantum systems, by focusing on essential similarities and differences rather than noise-induced fluctuations. For example, contrastive learning can mitigate the variability due to quantum measurements or excessive unitary rotations perturbed

by hardware imperfections. It can prioritize stable, intrinsic features over transient errors, thereby stabilizing feature extraction across noisy quantum circuits.

The layer-by-layer training approach complements the contrastive learning by sequentially optimizing the classical augmentation weights for each QFM layer. Rather than jointly training all parameters simultaneously using much more quantum resources for optimization, quantum resources are required only for data collection in our method. This strategy reduces computational complexity and avoids the pitfalls of gradient-based optimization in deep quantum circuits, such as barren plateaus [10–12], which are prevalent in VQAs.

We employ a supervised contrastive-learning protocol at each IQFMs layer  $l$  to leverage label information during training. Given a training example  $\mathbf{x}$  (or  $|\phi\rangle$ ) with true label  $y$ , we first compute its layer- $l$  augmented feature vector  $\mathbf{p}_l = \mathbf{h}_l$ , which serves as the anchor. We then sample a positive sample  $\mathbf{x}^+$  (or  $|\phi^+\rangle$ ) sharing the same label  $y$ , and a negative sample  $\mathbf{x}^-$  (or  $|\phi^-\rangle$ ) with a different label. Passing  $\mathbf{x}^+$  and  $\mathbf{x}^-$  through the first-layer QFM yields features  $\mathbf{g}_1^+$  and  $\mathbf{g}_1^-$ , which are then classically augmented by  $\mathbf{W}_1$  to produce

$$\mathbf{h}_1^+ = \mathcal{A}(\mathbf{W}_1, \mathbf{g}_1^+), \quad \mathbf{h}_1^- = \mathcal{A}(\mathbf{W}_1, \mathbf{g}_1^-). \quad (5)$$

We optimize  $\mathbf{W}_1$  by minimizing a contrastive loss  $\mathcal{C}(\mathbf{h}_1^+, \mathbf{h}_1^-)$ , thereby encouraging anchor–positive pairs to be closer than anchor–negative pairs in feature space. After convergence at layer 1, we fix  $\mathbf{W}_1$  and repeat the same procedure at layer 2 (training  $\mathbf{W}_2$  with new anchor, positive, and negative samples), and so on through layer  $L$ . This layer-wise training continues until a predefined criterion is met, enabling each  $\mathbf{W}_l$  to learn representations that maximize inter-class separability.

We utilize noise contrastive estimation [20] to address the minimization problem:

$$\mathbf{W}_l = \operatorname{argmin}_{\mathbf{W}_l} \frac{1}{N} \sum_{\mathbf{x}} \mathcal{C}(\mathbf{h}_l^+, \mathbf{h}_l^-), \quad (6)$$

where the cost function  $\mathcal{C}(\mathbf{h}_l^+, \mathbf{h}_l^-)$  is defined as:

$$\mathcal{C}(\mathbf{h}_l^+, \mathbf{h}_l^-) = \log \left[ 1 + \exp \left( \frac{\text{cs}(\mathbf{h}_l^-, \mathbf{p}_l) - \text{cs}(\mathbf{h}_l^+, \mathbf{p}_l)}{\tau} \right) \right]. \quad (7)$$

Here,  $\tau$  is the scale parameter, and  $\text{cs}$  denotes the cosine similarity function,  $\text{cs}(\mathbf{a}, \mathbf{b}) = \frac{\mathbf{a} \cdot \mathbf{b}}{\|\mathbf{a}\| \|\mathbf{b}\|}$ , where  $\mathbf{a} \cdot \mathbf{b}$  is the dot product and  $\|\mathbf{a}\|$ ,  $\|\mathbf{b}\|$  are the vector magnitudes. A similar form of Eq. (7) was employed in Ref. [39] for training deep physical neural networks. This cost is optimized using, for example, gradient descent for  $\mathbf{W}_l$  to bring the augmented vectors  $\mathbf{h}_l^+$  and  $\mathbf{p}_l$  closer together, while pushing  $\mathbf{h}_l^-$  and  $\mathbf{p}_l$  further apart. In the testing phase, the optimized IQFMs and classifier are applied sequentially to test data to predict labels.

In the representation learning, two types of training epochs are defined: outer training epochs and inner train-

ing epochs. During each outer epoch, the training samples are shuffled, and positive and negative pairs are selected for contrastive learning. Subsequently, inner epochs are performed to optimize the contrastive cost  $\mathcal{C}(\mathbf{h}_l^+, \mathbf{h}_l^-)$ . In all numerical experiments in our study, the scale parameter  $\tau$  is fixed at 8. The number of outer epochs is set to 100 for quantum data classification and 200 for classical data classification, while each outer epoch comprises 40 inner epochs.

### III. RESULTS

In this section, we numerically illustrate the effectiveness of IQFMs in classification tasks for both quantum data and classical data.

#### A. Quantum Data Classification

We perform two types of quantum phase recognition tasks to verify the versatility of IQFMs. These tasks aim to classify the ground states of Hamiltonians into several quantum phases. Quantum phase recognition is not only a standard benchmark in QML but also has potential applications in the field of condensed matter physics [40].

In the first task (Task A), we consider the following Hamiltonian on the one-dimensional  $n$ -qubit system with the periodic boundary condition [24]:

$$H_A = - \sum_{i=1}^n Z_i X_{i+1} Z_{i+2} - h_1 \sum_{i=1}^n X_i - h_2 \sum_{i=1}^n X_i X_{i+1}, \quad (8)$$

where  $h_1$  and  $h_2$  are constants, and  $Z_i$  and  $X_i$  are the Pauli matrices at the  $i$ th qubit. In this Hamiltonian, the competition of interactions gives rise to three distinct quantum phases: the symmetry-protected topological (SPT), paramagnetic, and anti-ferromagnetic phases [Fig. 4(a)]. Task A is a binary classification problem distinguishing the SPT phase from the other two phases. For training, we use 80 ground state wave functions. These are generated by sampling 40 evenly spaced values of  $h_1$  in the range  $[0, 1.6]$  for each of  $h_2 = 0$  and  $h_2 = -1.109$ . For testing, we use 800 test data points obtained by sampling 40 evenly spaced values of  $h_1$  in the range  $[0, 1.6]$  for each of the following  $h_2$  values:  $-1.35, -1.285, -1.225, -1.154, -1.109, -1.079, -1.049, -1.024, -1.0009, -1.004, -0.3531, -0.2479, -0.1377, -0.02755, 0.09766, 0.2229, 0.3631, 0.5033, 0.6636, 0.8439$ . Note that both the training and test datasets contain data for all three phases.

In the second task (Task B), we consider another one-dimensional Hamiltonian with the periodic bound-

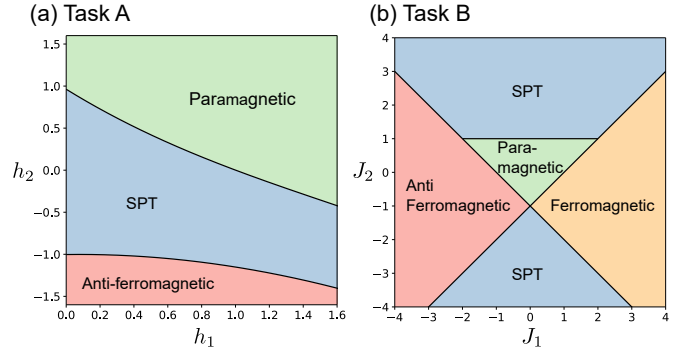


FIG. 4: Ground-state phase diagrams of Tasks A and B.

ary condition [41, 42]:

$$H_B = \sum_{i=1}^n Z_i - J_1 \sum_{i=1}^n X_i X_{i+1} - J_2 \sum_{i=1}^n X_{i-1} Z_i X_{i+1}, \quad (9)$$

where  $J_1$  and  $J_2$  are the coupling strengths. The phase diagram of this Hamiltonian includes the SPT, ferromagnetic, anti-ferromagnetic, and paramagnetic phases [Fig. 4(b)]. Task B is a four-class classification problem distinguishing all these quantum phases. We sample 50 and 1000 ground state wave functions for training and test datasets, respectively. For each dataset, the coupling constants  $J_1$  and  $J_2$  are randomly drawn from the range  $[-4, 4]$  and then fixed. We ensure an equal number of data for each class. These Hamiltonians are chosen to explore different quantum phase transitions and to evaluate the effectiveness of our proposed method in recognizing quantum phases. We fix  $n = 8$  and obtain the ground state wave functions by numerically diagonalizing the Hamiltonian matrices defined in Eqs. (8) and (9). These ground states are considered input states for IQFMs to predict their corresponding quantum phases. We generated these data based on Ref. [43].

The structure of IQFMs for this task is described in Fig. 5, where the embedding circuit  $\mathcal{U}_{\Psi(\mathbf{h}_{l-1})}$  and the preprocessing circuit  $P_l$  in each QFM layer consist of Hadamard and single- and two-qubit rotation gates. The embedding circuit is applied only from the second QFM layer onwards. After applying the embedding and preprocessing circuits, we extract the quantum features  $\mathbf{g}_l$  associated with  $n$  observables,  $O_i = Z_i$  ( $i = 1, \dots, n$ ), on four different measurement bases. That is, the dimension of the feature vector obtained in this process is  $d_g = 4n$ . Then, we classically augment  $\mathbf{g}_l$  as  $\mathbf{h}_l = \pi \tanh(\mathbf{W}_l \mathbf{g}_l / 2) \in \mathbb{R}^{d_g}$  and embed it into the next QFM layer, where  $\mathbf{W}_l$  is a  $d_g \times d_g$  matrix, and  $\tanh$  denotes the element-wise hyperbolic tangent function (note that  $d_g = d_h$ ). After obtaining  $\mathbf{h} = (\mathbf{h}_1, \dots, \mathbf{h}_L)$  from the representation learning, we train a three-layer feedforward NN to classify them into target phases. The numerical details of IQFMs are provided in Appendix A.

We compare the performance of IQFMs with the QCNN [24–26], which is a well-established QML model

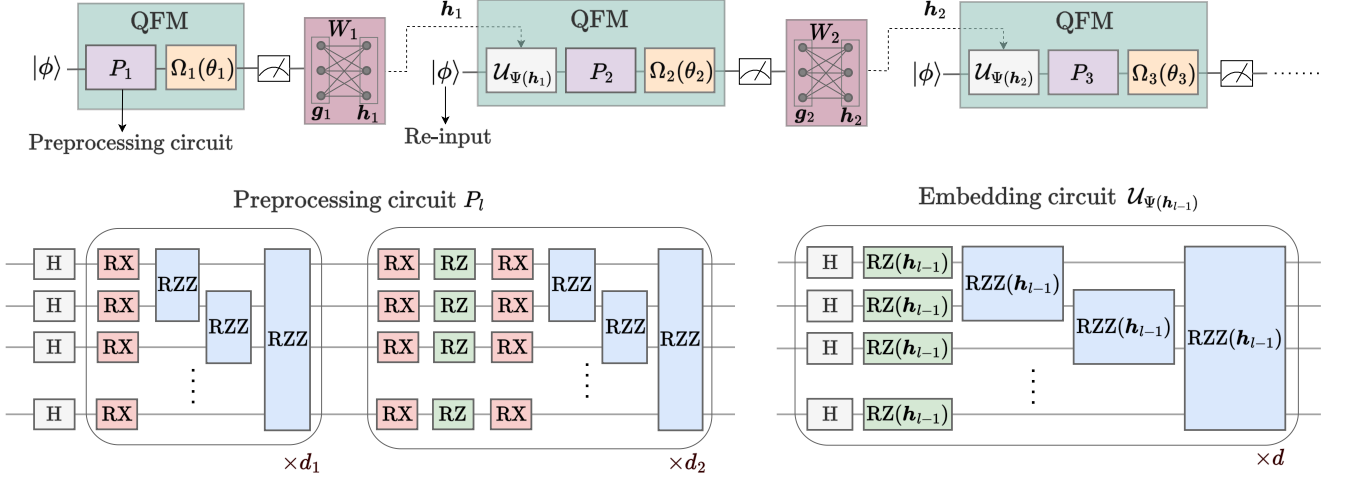


FIG. 5: For quantum data classification tasks, IQFMs incorporates a re-input structure:  $|\psi\rangle_0 = |\phi\rangle$  and  $|\psi\rangle_{l-1} = |\psi\rangle_0$  for  $l = 1, 2, \dots$ , where  $|\phi\rangle$  is the input quantum state. The  $l$ -th preprocessing circuit  $P_l$  starts with Hadamard gates applied to all qubits, followed by several layers of randomly parameterised RX, RZ, and RZZ gates. Starting from the second QFM layer, an embedding circuit  $U_{\Psi(h_{l-1})}$  maps classical data  $h_{l-1}$  into a quantum state. This circuit comprises  $d$  layers, each consisting of Hadamard gates on all qubits, followed by RZ and RZZ gates parameterized by  $h_{l-1}$ . In both the preprocessing and embedding circuits, RX and RZ gates are applied to each qubit individually, and RZZ gates are applied to all adjacent qubit pairs arranged in a circular topology.

for these tasks. The QCNN consists of alternating convolutional and pooling layers. The convolutional layers utilize single- and two-qubit rotation gates with variational parameters optimized during training to extract local features. The pooling layers reduce the number of active qubits by half until only one qubit remains. Finally, the expectation value of the Pauli-Z operator is measured to generate output for the classification task. The details of QCNN are provided in Appendix B. We use the TorchQuantum [44] library in our numerical experiments.

Figure 6 presents the test accuracy of IQFMs compared to QCNN, averaged over 50 experimental runs with different random initializations. Figures 6 (a) and (c) show the performance of IQFMs across various layer depths  $L$ , both with (contrastive) and without (non-contrastive) training the classical argumentation weights  $W_l$ . In non-contrastive case, the weights remain randomly initialized and untrained. Figures 6 (b) and (d) show the performance of QCNN for different convolutional layer depths, denoted as var\_depth. Here, the expectation values of observables are calculated exactly, corresponding to an infinite number of measurement shots. For both tasks, IQFMs consistently outperforms QCNN in terms of test accuracy, regardless of whether contrastive learning is used, even though the QFM circuits themselves are not optimized. These results suggest that quantum feature extraction via random measurement bases combined with classical post-processing is sufficiently powerful to learn the relevant quantum phases.

Figure 6 also highlights the benefits of contrastive

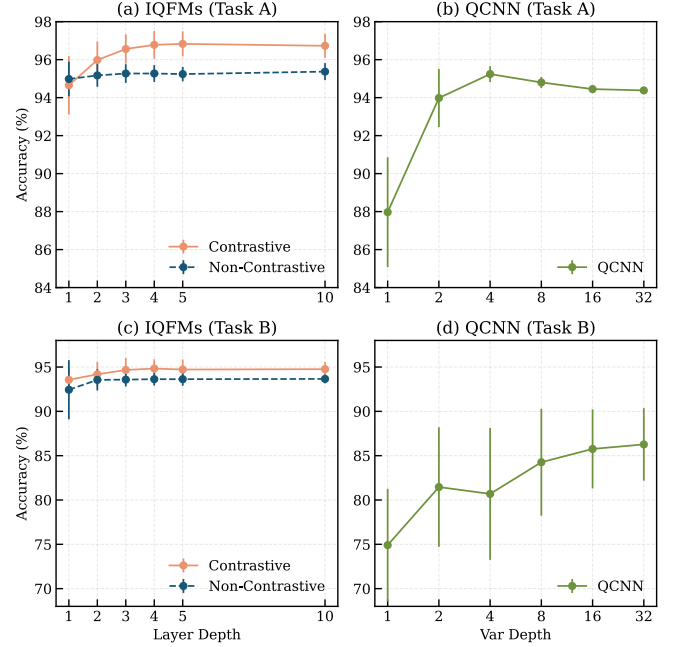


FIG. 6: Test accuracy for Tasks A and B using IQFMs and QCNN under different configurations. The solid orange lines, dashed teal-blue lines, and solid green lines represent the average accuracy over 50 trials (with error bars) for IQFMs with contrastive learning, IQFMs with non-contrastive learning, and QCNN, respectively.

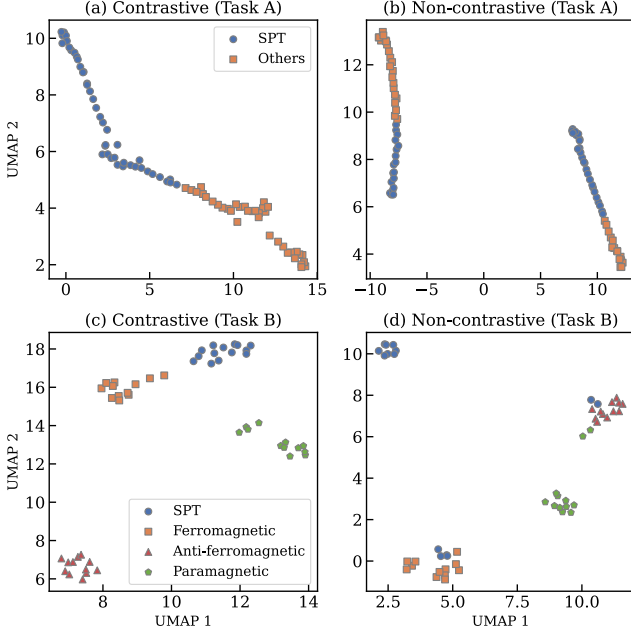


FIG. 7: Visualization of the final representation vectors from IQFMs using UMAP [45] for Tasks A and B. Each point represents a test sample, with a marker indicating the corresponding quantum phase.

learning for IQFMs. Training  $\mathbf{W}_l$  with contrastive learning improves the separability of quantum data associated with different quantum phases, leading to higher accuracy across most layer depths  $L$ . To further validate the effectiveness of contrastive learning instead of the post processing NN, we visualize the final representation vector  $(\mathbf{h}_1, \dots, \mathbf{h}_L) \in \mathbb{R}^{d_h L}$  from IQFM using Uniform Manifold Approximation and Projection (UMAP) technique [45] for both contrastive and non-contrastive cases, as shown in two-dimensional plots in Fig. 7. The results demonstrate that contrastive learning produces more cohesive clusters in the representation space, indicating more discriminative and effective representations.

Another remarkable advantage of IQFMs is its robustness against noise. To verify this, we evaluate the performance of IQFMs (with contrastive learning) under two types of noise: physical RX noise and statistical errors due to a limited number of measurement shots. For physical RX noise, we apply random RX rotations with angles in the range  $[0, 2\pi p]$  to the data, where  $p$  represents the noise level. In this setting, expectation values of observables are computed exactly, corresponding to an infinite number of measurement shots. Figure 8 presents the test accuracy of IQFMs with  $L = 5$  layers using contrastive learning compared to QCNN across various noise levels. While the accuracy of both models declines as the noise level increases, IQFMs consistently outperforms QCNN at most noise levels, especially at higher noise levels for both Tasks A and B.

We also investigate the impact of statistical errors arising

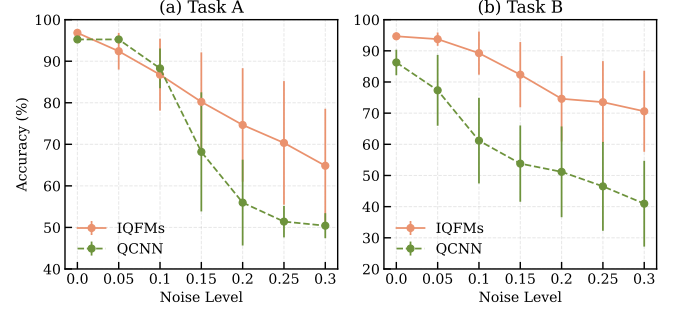


FIG. 8: Test accuracy for (a) Task A and (b) Task B of IQFMs and QCNN across different noise levels applied to the input data. The solid orange lines and dashed green lines represent the average accuracy over 50 trials (with error bars) for IQFMs (with contrastive learning) and QCNN, respectively.

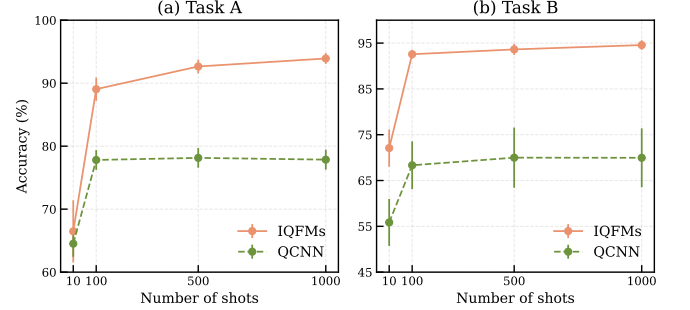


FIG. 9: Test accuracy for (a) Task A and (b) Task B of IQFMs and QCNN across different numbers of measurement shots. The solid orange lines and dashed green lines represent the average accuracy over 50 trials (with error bars) for IQFMs (with contrastive learning) and QCNN, respectively.

from a limited number of measurement shots. We conduct numerical experiments under finite-shot conditions, where expectation values of observables are estimated via sampling. Figure 9 shows the test accuracy for Task A and B, evaluated over 50 experimental runs with different random parameter initializations for both IQFMs and QCNN across various numbers of shots. The results indicate that IQFMs significantly achieves higher test accuracy than QCNN as the number of shots increases, even though a similar number of training epochs is considered for both methods. These findings suggest that IQFMs is more robust to both physical and statistical noise, making it a reliable choice for noisy real-world quantum data.

## B. Classical Data Classification

We demonstrate the effectiveness of IQFMs in classical data classification tasks, showing that it achieves perfor-



mance comparable to classical NNs with similar architectures. For evaluation, we use the Fashion-MNIST benchmark [46], a widely used dataset for machine learning, consisting of 60,000 training and 10,000 test samples of  $28 \times 28$  gray images of clothing items, each labeled with one of 10 classes. In this demonstration, we perform 10-class classification using 5,000 randomly selected training samples and 10,000 test samples for each run. In the contrastive learning setup, the augmented vector  $\mathbf{h}_l(\mathbf{x})$  of the input sample  $\mathbf{x}$  is set as the anchor vector  $\mathbf{p}_l$ . The positive sample  $\mathbf{x}^+$  is randomly selected from the training samples with the same label as  $\mathbf{x}$  and rotated 90 degrees. The negative sample  $\mathbf{x}^-$  is randomly selected from the training samples with a different label from  $\mathbf{x}$ .

To efficiently handle relatively large data, we adopt the modular IQFMs architecture illustrated in Fig. 2, where each module consists of  $\frac{M}{16}$  QFMs, and each QFM processes the 16-dimensional segment of classical data. Initially, the raw image data  $\mathbf{h}_{\text{raw}} \in \mathbb{R}^{28 \times 28} = \mathbb{R}^{784}$ , is linearly projected into an  $M$ -dimensional vector via  $\mathbf{h}_0 = \mathbf{W}_0 \mathbf{h}_{\text{raw}}$ , with  $\mathbf{W}_0 \in \mathbb{R}^{M \times 784}$ . The resulting vector  $\mathbf{h}_0$  is partitioned into  $\frac{M}{16}$  blocks of 16 dimensions, each fed into a different four-qubit QFM in the first module. Each QFM in  $l$ th layer is initialized in the state  $|\psi\rangle_l = |0\rangle^{\otimes 4}$  and implements the embedding circuit  $\mathcal{U}_{\Psi(\mathbf{h}_{l-1})}$  (as shown in Fig. 5), excluding the preprocessing circuit  $P_l$ . Quantum features are extracted via four Pauli-Z observables,  $O_i = Z_i$  ( $i = 1, \dots, 4$ ), measured in four different bases. This yields a  $d_g = 4 \times 4 \times \frac{M}{16} = M$ -dimensional feature vector  $\mathbf{g}_l$ . A classical augmentation step is then applied:  $\mathbf{h}_l = \pi \tanh(\mathbf{W}_l \mathbf{g}_l / 2) \in \mathbb{R}^M$ , where  $\mathbf{W}_l \in \mathbb{R}^{M \times M}$ . After the representation learning obtains  $(\mathbf{h}_1, \dots, \mathbf{h}_L)$ , a three-layer feedforward NN  $\mathcal{N}$  is trained to classify them into image classes.

For comparison, we also evaluate a classical NN with the same width  $M$  and depth  $L$ , in which the QFM modules are replaced by classical nonlinear activations. Specifically, each layer is defined by  $\mathbf{h}_l = \tanh(\mathbf{g}_l)$  with  $\mathbf{g}_l = \mathbf{W}_l \mathbf{h}_{l-1}$ . The representation learning is performed using this classical NN to produce the final feature vectors, which are then passed to the same downstream classifier  $\mathcal{N}$  for evaluation.

Figure 10 presents the test accuracy of classical neural networks and IQFMs models with  $L = 4$  layers and layer widths  $M = 16, 64$ , and  $256$ , evaluated over 50 independent runs with different random parameter initializations. As the layer width  $M$  increases, a consistent improvement in test accuracy is observed. The results also underscore the benefit of contrastive learning: IQFMs with contrastive learning consistently outperforms its non-contrastive counterpart. Although classical NNs are well-suited to classical image data, well-designed IQFMs can achieve comparable performance to its classical counterpart with similar architecture.

Combined with results on quantum data and classical data classification tasks, our findings highlight the versatility of the proposed method across both classical and quantum domains. As an alternative to the two-step

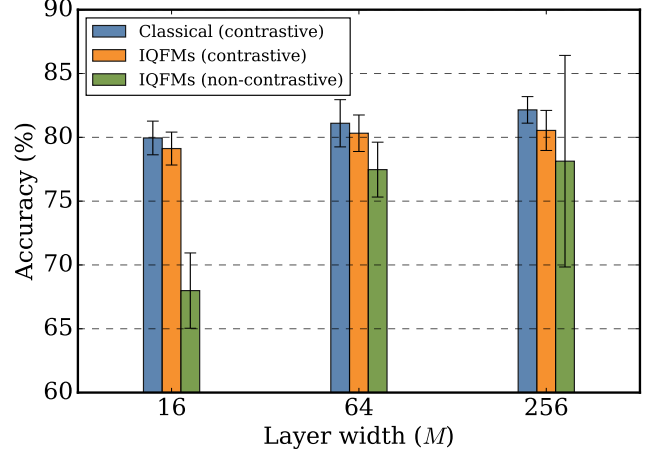


FIG. 10: Bar plot comparing the average test accuracy of the Fashion-MNIST classification as a function of layer width  $M$  for three models: the classical NN (teal blue), IQFMs with contrastive learning (orange), and IQFMs without contrastive learning (green). Each bar represents the mean accuracy over 50 independent runs, and the error bars indicate the standard deviation.

learning approach described in Fig. 1, there is a one-step learning method that employs contrastive learning using input samples that integrate both original data and labels; the details and results of this method are provided in Appendix C.

#### IV. CONCLUSION AND DISCUSSION

We have introduced the IQFMs, a hybrid quantum-classical framework designed to reduce the quantum resources required for learning compared to VQAs. This framework features a deep structure that iteratively connects shallow QFMs. By training only the classical augmentation weights between QFMs, rather than the variational parameters of the quantum circuits, this design significantly reduces quantum computational runtime. The IQFMs, with its feasibility for implementation on quantum hardware, emerges as a promising candidate for demonstrating QML applications on actual quantum devices for both classical and quantum data.

The use of contrastive learning to train the classical augmentation weights helps mitigate the effects of noise in the system. Numerical experiments demonstrate that IQFMs achieves superior test accuracy compared to QCNN in tasks involving the classification of noisy quantum data. Even in classical image classification tasks, IQFMs delivers performance comparable to similarly structured classical NNs. This approach offers a promising pathway to overcome current limitations and fully harness the potential of quantum-enhanced machine learning methods. Furthermore, contrastive learning is not limited to classification tasks; it can also be extended

to regression tasks [47], expanding its range and effectiveness for real-world applications.

An alternative biologically inspired training algorithm, direct feedback alignment (DFA) [48], can be considered for training the classical augmentation weights in the IQFMs. DFA leverages random projections combined with alternative nonlinear activation functions, particularly when the gradient of the primary activation function is difficult to evaluate. To adapt this approach to the quantum context, various activation functions can be selected, provided the correlation between these functions and the QFM output (treated as an activation) is not close to zero [49], offering a flexible and potentially robust training strategy.

The simplicity of back-propagation has established it as the standard method for training classical NNs. Since back-propagation requires storing intermediate activations during the forward pass to compute gradients in the backward pass, it is incompatible with learning quantum circuits, where such intermediate states are generally inaccessible [16, 17]. Without back-propagation, IQFMs relies on learning hierarchical intermediate representations that build upon one another, a concept rooted in the fundamental principles of deep learning. This enables the training of deep architectures to learn complex, hierarchical representations. One might question whether representation learning is essential. For instance, IQFMs can be redesigned to allow user-defined representations [50], offering more flexibility in its application.

## ACKNOWLEDGMENTS

The authors acknowledge Yuichi Kamata and Shintaro Sato for fruitful discussions. Special thanks are extended to Yuichi Kamata for his valuable comments on the training algorithm of IQFMs.

## Appendix A: IQFMs in quantum data classification

In IQFMs model, the  $l$ -th QFM block includes a preprocessing circuit  $P_l$  and an embedding circuit  $\mathcal{U}_{\Psi(\mathbf{h}_{l-1})}$  (Fig. 5). Here, let the symbols  $\alpha, \beta, \gamma, \epsilon, \zeta$  and  $\eta$  denote independent random rotation-angle parameters of the preprocessing circuit, which are fixed throughout the entire training and inference stages. The preprocessing circuit  $P_l$  with  $n$  qubits is defined as:

$$P_1 = \left( \prod_{r=1}^{d_2} B_r^{(1)} \right) \left( \prod_{r=1}^{d_1} A_r^{(1)} \right) H^{\otimes n},$$

$$P_l = \left( \prod_{r=1}^{d_2} B_r^{(l)} \right) H^{\otimes n}, \quad 2 \leq l \leq L, \quad (\text{A1})$$

where  $H^{\otimes n}$  is the Hadamard gates acting on all qubits, and  $L$  denotes the total number of layers in IQFMs. The

preprocessing circuit consists of two main components:  $A_r^{(1)}$  and  $B_r^{(l)}$ , which are defined as follows:

$$A_r^{(1)} = \exp \left( i \sum_{j=1}^n \alpha_{r,j} Z_j \otimes Z_{j+1} \right) \exp \left( i \sum_{j=1}^n \beta_{r,j} X_j \right),$$

$$B_r^{(l)} = \exp \left( i \sum_{j=1}^n \gamma_{r,j}^{(l)} Z_j \otimes Z_{j+1} \right) \exp \left( i \sum_{j=1}^n \epsilon_{r,j}^{(l)} X_j \right) \\ \times \exp \left( i \sum_{j=1}^n \zeta_{r,j}^{(l)} Z_j \right) \exp \left( i \sum_{j=1}^n \eta_{r,j}^{(l)} X_j \right), \quad (\text{A2})$$

where we have assumed the periodic boundary condition. In our numerical experiments, the depths of the layers in the preprocessing circuit are set to  $d_1 = 2$  and  $d_2 = 2$ .

The embedding circuit  $\mathcal{U}_{\Psi(\mathbf{h})}$  transforms classical data  $\mathbf{h}$  into a quantum state. We construct an embedding quantum circuit with  $n$  qubits and a depth of  $d$  layers ( $d = 4$  in our experiments) to embed  $\mathbf{h} = (h_1, h_2, \dots, h_{nd}) \in \mathbb{R}^{nd}$ . In a  $n$ -qubit feature map with depth  $d$ , the classical data  $\mathbf{h}$  is partitioned into  $d$  contiguous subvectors of length  $n$ :  $\mathbf{h}^{(m)} = (h_{n(m-1)+1}, \dots, h_{nm})$ ,  $m = 1, 2, \dots, d$ . Then, the embedding circuit is defined as:

$$\mathcal{U}_{\Psi(\mathbf{h})} = \prod_{m=1}^d \left[ \exp \left( -i \sum_{j=1}^n \frac{h_j^{(m)} h_{j+1}^{(m)}}{2} Z_j \otimes Z_{j+1} \right) \right. \\ \left. \times \exp \left( -i \sum_{j=1}^n \frac{h_j^{(m)}}{2} Z_j \right) H^{\otimes n} \right]. \quad (\text{A3})$$

After the representation learning stage, the feature vectors from all QFM layers,  $(\mathbf{h}_1, \dots, \mathbf{h}_L)$ , are concatenated and passed to a three-layer feedforward NN for classification. This network consists of an input layer for linear transformation, two hidden layers with ReLU activations, and an output layer with a Softmax function to produce class probabilities. The model is trained using the cross-entropy loss with the Adam optimizer [51] (learning rate: 0.001, weight decay:  $1e-4$ ) over 500 epochs. Training is performed in mini-batches, with loss computed and gradients propagated for parameter updates. The early stopping procedure is employed to prevent overfitting.

## Appendix B: QCNN in quantum data classification

The QCNN model used in our numerical experiments consists of alternating convolutional and pooling layers. The convolutional layers apply multiple quantum operations to the input qubits, consisting of sequential RX, RZ, and RX gates followed by RZZ gates between adjacent qubits. Each gate is parameterized by trainable variational parameters, which are optimized during training.

These operations are repeated for a specified number of layers, denoted by `var_depth`. Pooling layers use CNOT gates to entangle qubits and reduce the number of active qubits by half, continuing recursively until only one qubit remains. The final output is obtained by measuring the expectation value of the Pauli-Z operator on this remaining qubit. For binary classification (Task A), model performance is evaluated using mean squared error. For multi-class classification (Task B), a fully connected classical layer is appended to map the circuit output to a vector with a number of elements equal to the number of classes. Then, cross-entropy loss is used by comparing predicted logits to integer-encoded labels.

Figures 6 and 8 present results under the assumption of an infinite number of measurement shots. We use the Adam optimizer [51] with a learning rate of 0.001 and weight decay of  $1e-5$ , over 1000 epochs for Task A and 5000 epochs for Task B. Under a finite-shot setting (Fig. 9), the parameter-shift rule is employed with mini-batch stochastic gradient descent. The batch sizes are set to 4 for Task A and 5 for Task B, with learning rates of 0.001 for both tasks, and training is performed over 300 epochs for both tasks. The early stopping procedure is employed to prevent overfitting. The `var_depth` of QCNN is set to 4 for Task A and 32 for Task B in Fig. 8, and 4 for both tasks in Fig. 9.

### Appendix C: IQFMs with one-step learning

We introduce an alternative training scheme for IQFMs, referred to as the one-step learning method, which employs contrastive learning using input samples that integrate both original data and labels. This method is compared with the two-step learning approach described in the main text with Fig. 1. In one-step learning, each input sample  $\mathbf{x}$  consists of a data component  $\mathbf{s}$  and its corresponding label  $\mathbf{y}$ . A positive sample  $\mathbf{x}^+ = (\mathbf{s}, \mathbf{y})$  is paired with a negative sample  $\mathbf{x}^- = (\mathbf{s}, \tilde{\mathbf{y}})$ , where  $\tilde{\mathbf{y}}$  denotes an incorrect label. The anchor vector  $\mathbf{p}_l$  is set as a fixed random vector for each layer  $l$ .

During training, the contrastive loss function in Eq. (7) is optimized using the augmented feature vectors  $\mathbf{h}_1(\mathbf{x}^+)$ ,  $\mathbf{h}_1(\mathbf{x}^-)$ , and the anchor  $\mathbf{p}_l$ . In the inference phase, given a new data input  $\mathbf{s}$ , the model predicts its label by evaluating candidate labels  $\mathbf{y}_1, \dots, \mathbf{y}_K$ . For each label  $\mathbf{y}_k$ , an input sample  $\mathbf{x}_k = (\mathbf{s}, \mathbf{y}_k)$  is formed, and a cumulative similarity score is computed across all layers as  $C_k = \sum_l \text{cs}(\mathbf{h}_l(\mathbf{x}_k), \mathbf{p}_l)$ . The predicted label corresponds to the index  $k$  that maximizes  $C_k$ .

For quantum phase recognition tasks, the input-label integration is realized by constructing a joint input state  $|\phi\rangle \otimes |\text{label}\rangle$ , where  $|\phi\rangle$  is the input quantum data and  $|\text{label}\rangle$  is a quantum encoding of the one-hot label.

Figure 11 presents the test accuracy of IQFMs using both the two-step and one-step learning methods, evaluated across varying layer depths. All other parameters

follow the configurations described in Appendix A. In the

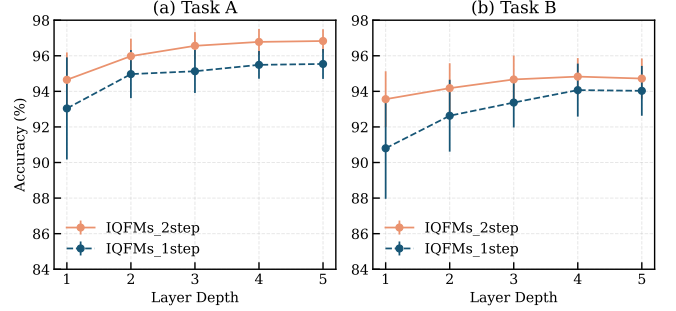


FIG. 11: Test accuracy for (a) Task A and (b) Task B of IQFMs with two-step learning and IQFMs with one-step learning across different layer depths. The solid orange lines and dashed teal-blue lines represent the average accuracy over 50 trials (with error bars) for IQFMs with two-step learning and IQFMs with one-step learning, respectively.

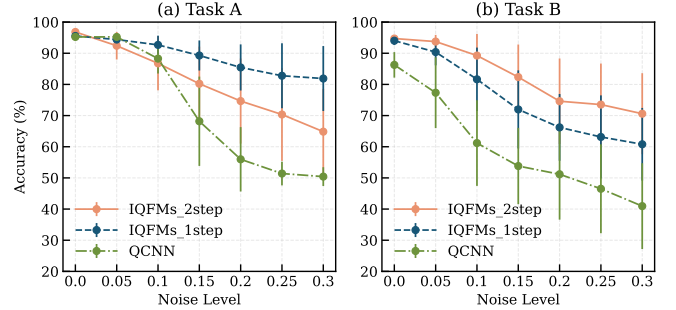


FIG. 12: Test accuracy for (a) Task A and (b) Task B of IQFMs with two-step learning, IQFMs with one-step learning and QCNN across different noise levels. The solid orange lines, dashed teal-blue lines and dash-dot green lines represent the average accuracy over 50 trials (with error bars) for IQFMs with two-step learning, IQFMs with one-step learning and QCNN, respectively.

absence of noise, two-step learning consistently outperforms one-step learning across different depths.

Figure 12 shows the test accuracy of IQFMs ( $L = 5$  layers) with two-step learning, IQFMs with one-step learning, and QCNN under varying noise levels, assuming an infinite number of measurement shots. The `var_depth` of QCNN is set to 4 for Task A and 32 for Task B. All other parameters follow the configurations described in Appendices A and B. The results reveal that both one-step and two-step IQFMs outperform QCNN. Interestingly, the relative performance of one-step and two-step learning depends on the task and noise conditions. Under high noise levels, one-step learning outperforms for Task A, while two-step learning remains more effective for Task B.

- [1] V. Havlíček, A. D. Córcoles, K. Temme, A. W. Harrow, A. Kandala, J. M. Chow, and J. M. Gambetta, Supervised learning with quantum-enhanced feature spaces, *Nature* **567**, 209 (2019).
- [2] M. Schuld and N. Killoran, Quantum machine learning in feature Hilbert spaces, *Phys. Rev. Lett.* **122**, 040504 (2019).
- [3] S. Bravyi, D. Gosset, and R. König, Quantum advantage with shallow circuits, *Science* **362**, 308–311 (2018).
- [4] Y. Liu, S. Arunachalam, and K. Temme, A rigorous and robust quantum speed-up in supervised machine learning, *Nat. Phys.* (2021).
- [5] T. Goto, Q. H. Tran, and K. Nakajima, Universal approximation property of quantum machine learning models in quantum-enhanced feature spaces, *Phys. Rev. Lett.* **127**, 090506 (2021).
- [6] H.-Y. Huang, M. Broughton, M. Mohseni, R. Babbush, S. Boixo, H. Neven, and J. R. McClean, Power of data in quantum machine learning, *Nat. Commun.* **12**, 2631 (2021).
- [7] K. Mitarai, M. Negoro, M. Kitagawa, and K. Fujii, Quantum circuit learning, *Phys. Rev. A* **98**, 032309 (2018).
- [8] E. R. Anschuetz and B. T. Kiani, Quantum variational algorithms are swamped with traps, *Nat. Commun.* **13**, 7760 (2022).
- [9] L. Bittel and M. Kliesch, Training variational quantum algorithms is np-hard, *Phys. Rev. Lett.* **127**, 120502 (2021).
- [10] J. R. McClean, S. Boixo, V. N. Smelyanskiy, R. Babbush, and H. Neven, Barren plateaus in quantum neural network training landscapes, *Nat. Commun.* **9**, 4812 (2018).
- [11] M. Cerezo, A. Sone, T. Volkoff, L. Cincio, and P. J. Coles, Cost function dependent barren plateaus in shallow parametrized quantum circuits, *Nat. Commun.* **12**, 1791 (2021).
- [12] C. Ortiz Marrero, M. Kieferová, and N. Wiebe, Entanglement-induced barren plateaus, *PRX Quantum* **2**, 040316 (2021).
- [13] E. Gil-Fuster, C. Gyurik, A. Pérez-Salinas, and V. Dunjko, On the relation between trainability and dequantization of variational quantum learning models, arXiv [10.48550/arXiv.2406.07072](https://arxiv.org/abs/10.48550/arXiv.2406.07072) (2024).
- [14] P. Bermejo, P. Braccia, M. S. Rudolph, Z. Holmes, L. Cincio, and M. Cerezo, Quantum convolutional neural networks are (effectively) classically simulable, arXiv [10.48550/arXiv.2408.12739](https://arxiv.org/abs/10.48550/arXiv.2408.12739) (2024).
- [15] S. Lerch, R. Puig, M. S. Rudolph, A. Angrisani, T. Jones, M. Cerezo, S. Thanasilp, and Z. Holmes, Efficient quantum-enhanced classical simulation for patches of quantum landscapes, arXiv [10.48550/arXiv.2411.19896](https://arxiv.org/abs/10.48550/arXiv.2411.19896) (2024).
- [16] A. Abbas, R. King, H.-Y. Huang, W. J. Huggins, R. Movassagh, D. Gilboa, and J. McClean, On quantum backpropagation, information reuse, and cheating measurement collapse, in *Advances in Neural Information Processing Systems*, Vol. 36 (2023).
- [17] K. Chinzei, S. Yamano, Q. H. Tran, Y. Endo, and H. Oshima, Trade-off between gradient measurement efficiency and expressivity in deep quantum neural networks, *npj Quantum Inf.* **11**, 79 (2025).
- [18] H.-Y. Liu, Z.-Y. Chen, T.-P. Sun, C. Xue, Y.-C. Wu, and G.-P. Guo, Can variational quantum algorithms demonstrate quantum advantages? time really matters, arXiv [10.48550/arxiv.2307.04089](https://arxiv.org/abs/10.48550/arxiv.2307.04089) (2023).
- [19] R. Hadsell, S. Chopra, and Y. LeCun, Dimensionality reduction by learning an invariant mapping, in *Proc. IEEE Conf. Comput. Vis. Pattern Recognit. (CVPR)*, Vol. 2 (IEEE, 2006) pp. 1735–1742.
- [20] M. Gutmann and A. Hyvärinen, Noise-contrastive estimation: A new estimation principle for unnormalized statistical models, in *Proc. 13th Int. Conf. Artif. Intell. Stat.*, Vol. 9 (PMLR, 2010) pp. 297–304.
- [21] A. van den Oord, Y. Li, and O. Vinyals, Representation learning with contrastive predictive coding, arXiv [10.48550/arXiv.1807.03748](https://arxiv.org/abs/10.48550/arXiv.1807.03748) (2018).
- [22] K. He, H. Fan, Y. Wu, S. Xie, and R. Girshick, Momentum contrast for unsupervised visual representation learning, in *Proc. IEEE Conf. Comput. Vis. Pattern Recognit. (CVPR)* (IEEE, 2020) pp. 9729–9738.
- [23] T. Chen, S. Kornblith, M. Norouzi, and G. Hinton, A simple framework for contrastive learning of visual representations, in *Proc. 37th Int. Conf. Mach. Learn. (ICML)*, Vol. 119, edited by H. D. III and A. Singh (PMLR, 2020) pp. 1597–1607.
- [24] I. Cong, S. Choi, and M. D. Lukin, Quantum convolutional neural networks, *Nature Physics* **15**, 1273 (2019).
- [25] K. Chinzei, Q. H. Tran, K. Maruyama, H. Oshima, and S. Sato, Splitting and parallelizing of quantum convolutional neural networks for learning translationally symmetric data, *Phys. Rev. Res.* **6**, 023042 (2024).
- [26] K. Chinzei, Q. H. Tran, Y. Endo, and H. Oshima, Resource-efficient equivariant quantum convolutional neural networks, [arXiv:2410.01252 \[quant-ph\]](https://arxiv.org/abs/2410.01252) (2024).
- [27] A. Pérez-Salinas, A. Cervera-Lierta, E. Gil-Fuster, and J. I. Latorre, Data re-uploading for a universal quantum classifier, *Quantum* **4**, 226 (2020), [1907.02085](https://arxiv.org/abs/1907.02085).
- [28] X. Gao, E. R. Anschuetz, S.-T. Wang, J. I. Cirac, and M. D. Lukin, Enhancing generative models via quantum correlations, *Phys. Rev. X* **12**, 021037 (2022).
- [29] M. S. Rudolph, N. B. Toussaint, A. Katabarwa, S. Johri, B. Peropadre, and A. Perdomo-Ortiz, Generation of high-resolution handwritten digits with an ion-trap quantum computer, *Phys. Rev. X* **12**, 031010 (2022).
- [30] M. Van Den Nest, Simulating quantum computers with probabilistic methods, *Quantum Info. Comput.* **11**, 784–812 (2011).
- [31] M. Schuld, V. Bergholm, C. Gogolin, J. Izaac, and N. Killoran, Evaluating analytic gradients on quantum hardware, *Phys. Rev. A* **99**, 032331 (2019).
- [32] G.-B. Huang, Q.-Y. Zhu, and C.-K. Siew, Extreme learning machine: Theory and applications, *Neurocomputing* **70**, 489 (2006).
- [33] P. Mujal, R. Martínez-Peña, J. Nokkala, J. García-Bení, G. L. Giorgi, M. C. Soriano, and R. Zambrini, Opportunities in quantum reservoir computing and extreme learning machines, *Adv. Quantum Technol.*, 2100027 (2021).
- [34] K. Fujii and K. Nakajima, Harnessing disordered-ensemble quantum dynamics for machine learning, *Phys.*



- [Rev. Applied](#) **8**, 024030 (2017).
- [35] K. Nakajima, K. Fujii, M. Negoro, K. Mitarai, and M. Kitagawa, Boosting computational power through spatial multiplexing in quantum reservoir computing, [Phys. Rev. Applied](#) **11**, 034021 (2019).
  - [36] Q. H. Tran and K. Nakajima, Learning temporal quantum tomography, [Phys. Rev. Lett.](#) **127**, 260401 (2021).
  - [37] T. Kubota, Y. Suzuki, S. Kobayashi, Q. H. Tran, N. Yamamoto, and K. Nakajima, Temporal information processing induced by quantum noise, [Phys. Rev. Res.](#) **5**, 023057 (2023).
  - [38] Q. H. Tran and K. Nakajima, Higher-order quantum reservoir computing, [Preprint at arXiv:2006.08999](#) (2020).
  - [39] A. Momeni, B. Rahmani, M. Malléjac, P. del Hougne, and R. Fleury, Backpropagation-free training of deep physical neural networks, [Science](#) **382**, 1297–1303 (2023).
  - [40] D. Wu, R. Rossi, F. Vicentini, N. Astrakhantsev, F. Becca, X. Cao, J. Carrasquilla, F. Ferrari, A. Georges, M. Hibat-Allah, M. Imada, A. M. Läuchli, G. Mazzola, A. Mezzacapo, A. Millis, J. Robledo Moreno, T. Neupert, Y. Nomura, J. Nys, O. Parcollet, R. Pohle, I. Romero, M. Schmid, J. M. Silvester, S. Sorella, L. F. Tocchio, L. Wang, S. R. White, A. Wietek, Q. Yang, Y. Yang, S. Zhang, and G. Carleo, Variational benchmarks for quantum many-body problems, [Science](#) **386**, 296 (2024).
  - [41] R. Verresen, R. Moessner, and F. Pollmann, One-dimensional symmetry protected topological phases and their transitions, [Phys. Rev. B](#) **96**, 165124 (2017).
  - [42] N. Schuch, D. Pérez-García, and I. Cirac, Classifying quantum phases using matrix product states and projected entangled pair states, [Phys. Rev. B](#) **84**, 165139 (2011).
  - [43] E. Recio-Armengol, F. J. Schreiber, J. Eisert, and C. Bravo-Prieto, Learning complexity gradually in quantum machine learning models, [arXiv 10.48550/arXiv.2411.11954](#) (2024).
  - [44] H. Wang, Y. Ding, J. Gu, Y. Lin, D. Z. Pan, F. T. Chong, and S. Han, Quantumnas: Noise-adaptive search for robust quantum circuits, in [Proc. 28th IEEE Int. Symp. High-Perform. Comput. Arch., HCA '28](#) (2022).
  - [45] L. McInnes, J. Healy, and J. Melville, Umap: Uniform manifold approximation and projection for dimension reduction, [arXiv 10.48550/arXiv.1802.03426](#) (2018).
  - [46] H. Xiao, K. Rasul, and R. Vollgraf, Fashion-mnist: a novel image dataset for benchmarking machine learning algorithms, [arXiv 10.48550/arXiv.1708.07747](#) (2017).
  - [47] K. Zha, P. Cao, J. Son, Y. Yang, and D. Katabi, Rank-n-contrast: learning continuous representations for regression, in [Proc. 37th Int. Conf. on Neural Info. Process. Systems](#), NIPS '23 (Curran Associates Inc., Red Hook, NY, USA, 2023).
  - [48] A. Nøkland, Direct feedback alignment provides learning in deep neural networks, in [Proc. 30th Int. Conf. on Neural Info. Process. Systems](#), NIPS'16 (Curran Associates Inc., Red Hook, NY, USA, 2016) p. 1045–1053.
  - [49] M. Nakajima, K. Inoue, K. Tanaka, Y. Kuniyoshi, T. Hashimoto, and K. Nakajima, Physical deep learning with biologically inspired training method: gradient-free approach for physical hardware, [Nat. Commun.](#) **13**, 7847 (2022).
  - [50] Q. Li, Y. W. Teh, and R. Pascanu, Noprop: Training neural networks without back-propagation or forward-propagation, [arXiv 10.48550/arXiv.2503.24322](#) (2025).
  - [51] D. P. Kingma and J. Ba, Adam: A method for stochastic optimization, in [Proc. 3rd Int. Conf. on Learning Representations](#), ICLR '15 (2015).